Energy & Environmental Science

ROYAL SOCIETY OF CHEMISTRY

PAPER

View Article Online
View Journal | View Issue

Cite this: *Energy Environ. Sci.*, 2025, **18**, 1920

All-inorganic $CsPbI_2Br$ perovskite solar cells with thermal stability at 250 °C and moisture-resilience *via* polymeric protection layers†

Rajarshi Roy,[a] Mahdi Malekshahi Byranvand,*[a] Mohamed Reza Zohdi,[a] Theresa Magorian Friedlmeier,[c] Chittaranjan Das,[a] Wolfram Hempel,[c] Weiwei Zuo,[a] Mayank Kedia,[ab] Jose Jeronimo Rendon,[a] Stephan Boehringer,[a] Bekele Hailegnanw,[a] Michael Vorochta,[e] Sascha Mehl,[f] Monika Rai,‡[a] Ashish Kulkarni,*[bd] Sanjay Mathur[d] and Michael Saliba*[ab]

Received 31st May 2024,
Accepted 17th December 2024

DOI: 10.1039/d4ee02385d

rsc.li/ees

All-inorganic perovskites, such as $CsPbI_2Br$, have emerged as promising compositions due to their enhanced thermal stability. However, they face significant challenges due to their susceptibility to humidity. In this work, $CsPbI_2Br$ perovskite is treated with poly(3-hexylthiophen-2,5-diyl) (P3HT) during the crystallization resulting in significant stability improvements against thermal, moisture and steady-state operation stressors. The perovskite solar cell retains ~90% of the initial efficiency under relative humidity (RH) at ~60% for 30 min, which is among the most stable all-inorganic perovskite devices to date under such harsh conditions. Furthermore, the P3HT treatment ensures high thermal stress tolerance at 250 °C for over 5 h. In addition to the stability enhancements, the champion P3HT-treated device shows a higher power conversion efficiency (PCE) of 13.5% compared to 12.7% (reference) with the stabilized power output (SPO) for 300 s. In addition, the P3HT-protected perovskite layer in ambient conditions shows ~75% of the initial efficiency compared to the unprotected devices with ~28% of their initial efficiency after 7 days of shelf life.

Broader context

Metal halide perovskites have achieved a significant milestone by reaching >26% efficiency in recent years. Along with that, the remarkable stability improvement of perovskite solar cells (PSCs) makes it of interest for industry. All-inorganic perovskite solar cells have emerged as a promising candidates due to its robustness against heat. However, the stability against humidity remains a major concern. In this article, we use a polymeric overlayer to protect the perovskite absorber. We demonstrate the efficacy of our approach using various stability tests under high temperature and high humidity along with direct exposure of the perovskite films to water.

[a] *Institute for Photovoltaics (ipv), University of Stuttgart, 70569 Stuttgart, Germany. E-mail: mahdi.malekshahi@ipv.uni-stuttgart.de, michael.saliba@ipv.uni-stuttgart.de*

[b] *Helmholtz Young Investigator Group FRONTRUNNER, IEK-5 Photovoltaics, Forschungszentrum Jülich, 52425 Jülich, Germany. E-mail: a.kulkarni@fz-juelich.de*

[c] *Zentrum für Sonnenenergie- und Wasserstoff-Forschung (ZSW), 70563, Stuttgart, Germany. E-mail: theresa.friedlmeier@zsw-bw.de, wolfram.hempel@zsw-bw.de*

[d] *Institute of Inorganic and Materials Chemistry, University of Cologne, Greinstr. 6, 50939 Cologne, Germany*

[e] *Faculty of Mathematics and Physics, Charles University, V Holešovičkách 2, 18000 Prague, Czech Republic*

[f] *Elettra Sincrotrone, Strada Statale 14 km, 34149 Basovizza, Trieste, Italy*

† Electronic supplementary information (ESI) available. See DOI: https://doi.org/10.1039/d4ee02385d

‡ Current adress: Institute for Materials Research (IMO-IMOMEC), University of Hasselt, 3590 Diepenbeek, Belgium.

Introduction

Perovskite solar cells (PSCs) have garnered significant interest due to their excellent optoelectronic properties and high power conversion efficiencies (PCEs), which have increased from 3.8%[1] in 2009 to >26%[2] to date. The potential commercial viability of this technology is being evaluated due to recent advances in perovskite material, structural, and environmental stability achieved through compositional, interfacial, and additive engineering.[3–15] While improvements have been made in the moisture stability of organic–inorganic perovskites, concerns about low thermal stability persist, particularly due to the presence of volatile organic cations.[16] This concern has led to increased research on all-inorganic perovskites incorporating

the cesium (Cs) cation ($CsPbX_3$; X = I^-, Br^-). Recent studies have achieved relatively high PCEs for $CsPbI_3$[17,18] and $CsPbI_2Br$[19,20] PSCs of 19.6% and 17.8%, respectively. However, stability concerns persist. To increase confidence in the principled long-term thermal stability of PSCs, stability against extreme temperatures >400 °C, as achievable by all-inorganic perovskites, would be an important milestone. This could also be of potential interest for space applications. In addition to the thermal stability traits, demonstrating stability against moisture would be crucial in order to verify interface engineering strategies.

At the same time, apart from thermal degradation or chemical decomposition in a humid environment, there is also an inherent instability of the photoactive phase of all-inorganic perovskites at room temperature: Among the $CsPbX_3$ perovskite compositions, $CsPbI_3$ (bandgap of 1.7 eV) exhibits a phase instability at room temperature, *i.e.* a transition from the photoactive black phase (α) to the photoinactive yellow phase (δ).[21] $CsPbBr_3$ (bandgap of 2.3 eV), on the other hand, absorbs poorly beyond 540 nm.[22,23] As a trade-off, a mixed-halide $CsPbI_2Br$ composition shows a lower bandgap of 1.9 eV (with Shockley–Queisser limit of 24.7%) and better phase stability than $CsPbI_3$, thus positioning it as a promising candidate for thermally stable single-junction PSCs or multijunction applications.[24] While studies have shown improvements in phase stability,[25–33] achieving stability against moisture (full exposure to water) and heat (>200 °C) remains challenging, necessitating the development of innovative strategies to address these challenges.

In this study, we present an effective strategy to enhance the moisture and thermal stability of the $CsPbI_2Br$ perovskite films through polymer additive-assisted antisolvent engineering. An optimized amount of poly(3-hexylthiophen-2,5-diyl) (P3HT) polymer is introduced during the antisolvent dripping step, improving the perovskite crystallization. Our characterizations confirm the formation of a thin P3HT layer and the formation of CH_3Br-organic adduct on the surface of the perovskite film. This may also contribute to the enhancement of the interfacial junction between the perovskite and the HTL, leading to a device stability improvement. This may stem from the reduction of dangling bonds on the surface of the perovskite film, thus achieving a better interface. Upon exposure to moisture at relative humidity (RH) ~60% for 30 min, the devices retained 90% of their initial PCE. Additionally, when subjected to heating at 250 °C under ambient conditions for 300 min the devices retained ~50% of their initial PCE underlining the necessity for protection against moisture. Furthermore, the shelf life stability data demonstrates that, on average, the devices retained ~75% of their initial PCE for 7 consecutive days of measurement under 1-sun condition. The P3HT-treated device exhibited a notable enhancement in the fill factor (FF), >82%, compared to the reference device (without any treatment) with a FF of 79% underlining the improved interface resulting from the P3HT treatment.

Results and discussions

As shown in Scheme 1, our results are based on an n–i–p stack of indium tin oxide (ITO) glass/nanoparticle-based SnO_2 electron transport layer (ETL)/$CsPbI_2Br$ film (with and without P3HT-protection)/P3HT HTL/gold metal electrode. For the P3HT-protected devices, varying concentrations of P3HT in chlorobenzene (CB) are dissolved and dripped (as an antisolvent) during the perovskite precursor spin coating step, followed by annealing at 160 °C on a hot plate to facilitate perovskite crystallization. This modification leads to the formation of a P3HT protection layer at the interface between the perovskite and HTL.

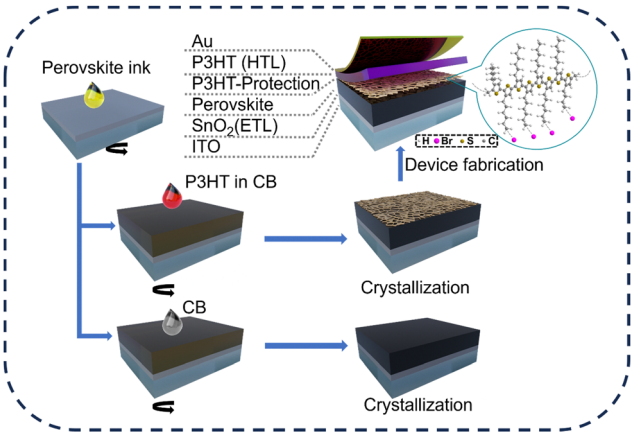

Scheme 1 Schematic illustration of perovskite film processing and perovskite device with and without P3HT-protection layer.

For P3HT-protection layer modification, from various film characterizations such as the X-ray diffraction (XRD) (Fig. S1, ESI†), scanning electron microscope (SEM) top-view (Fig. S2, ESI†), and from the device statistics (Fig. S3, ESI†) 6 mg mL^{-1} of P3HT-protection layer concentration was found to be the optimum and carried on for further characterizations. From here, for convenience, the perovskite devices and films modified with this P3HT interlayer concentration are referred to as "P3HT-protected" in comparison to the unmodified one as "unprotected".

To analyse the influence of P3HT-protection layer on the perovskite layer absorbance, we carried out UV-vis absorption measurements. The absorption spectra in Fig. 1(A) show no change in absorbance between the unprotected and the P3HT-protected substrates, indicating that the P3HT-protection layer at varying concentrations does not affect the optical properties of perovskite film (Fig. S4, ESI†). Additionally, the XRD measurement (Fig. 1(B)) reveals major characteristic peaks at 2θ = 14.6° and 29.8°, corresponding to the α-phase of the perovskite, with no traces of δ-phase at ~10°. Interestingly, the perovskite peak intensity is slightly higher with lower Full Width at Half Maximum (FWHM) (Fig. S5, ESI†) for the P3HT-protected compared to the unprotected. We posit that this is primarily due to the formation of a better interface between the perovskite absorber layer and the HTL by the P3HT treatment. This additionally results in a perovskite layer with fewer defects, leading to better crystallinity. From the SEM images in Fig. 1(C), the unprotected film exhibits a non-flat surface with high coverage, which transforms into a fully covered morphology with the addition of the P3HT layer on top of it (Fig. 1(D)). The effect of the P3HT protection over the perovskite

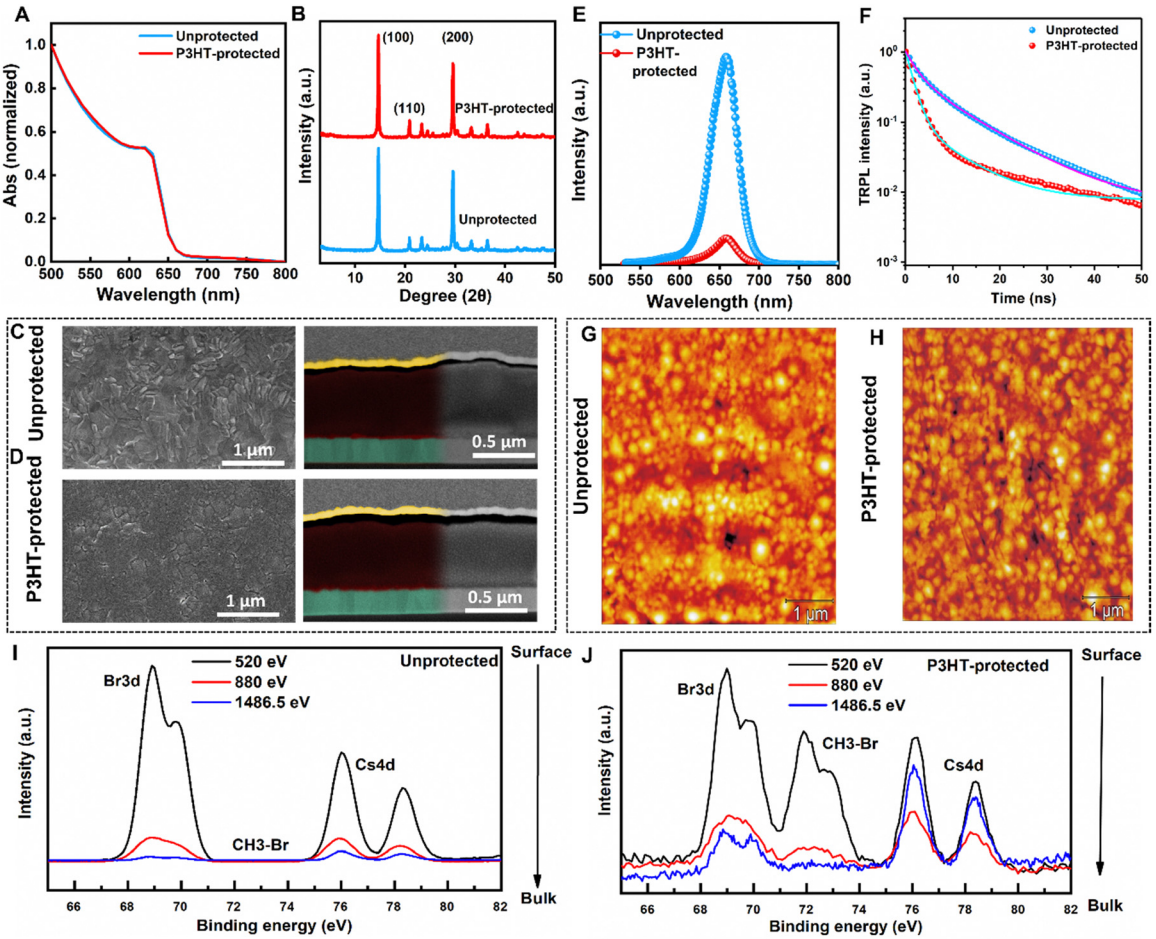

Fig. 1 (A) UV-Vis absorption spectra of unprotected film and P3HT-protected film, (B) XRD spectra (C) and (D) surface and cross-sectional SEM images, (E) steady-state PL spectra, (F) TRPL spectra, (G) and (H) AFM images of the unprotected and P3HT-protected films, (I) and (J) XPS measurement of Cs (4d) Br (3d) at 520 eV, 880 eV and 1486.5 eV for the unprotected film and P3HT-protected film.

layer is further evident from the atomic force microscopy (AFM) images for the unprotected and P3HT-protected films in Fig. 1(G) and (H). The root mean square (RMS) roughness of the perovskite film has decreased from 18 ± 1 nm for the unprotected to 12 ± 1 nm for the P3HT-protected approach. The improved uniformity is further verified by the surface SEM as shown in Fig. S6 (ESI†). In comparison to unprotected perovskite film (with an average grain size of 104 nm), the P3HT-protected film has shown a smaller grain size of 95 nm which is consistent with the improved interface for the P3HT route. Photoluminescence (PL) measurements were carried out to quantify the charge transport properties at the perovskite and P3HT interface. As depicted in Fig. 1(E), the P3HT-protected film shows significant PL quenching compared to the unprotected film, suggesting fast charge extraction attributable to the P3HT-protection layer compared to the unprotected film. This is further corroborated by the time-resolved photoluminescence (TRPL) measurement: TRPL measurement is performed to further understand the carrier transfer dynamics at the perovskite/HTL interface, and the results are shown in Fig. 1(F). The TRPL curves are fitted with the biexponential decay function as shown in Table S1 (ESI†).

$$I(t) = A_1 \exp\left(-\frac{t}{\tau_1}\right) + A_2 \exp\left(-\frac{t}{\tau_2}\right) + K$$

Here, A_1 and A_2 are the decay amplitude, τ_1 and τ_2 are the characteristic time constants for the first and second exponential decays, respectively. K is a constant for the base-line offset. Here we emphasize that the characteristic time constants which are obtained from the biexponential fitting, solely represent the fitting parameters which are further used to understand the PL decay for the unprotected and P3HT-proteted films. Here during the analysis, τ_1 and τ_2 are attributed to the characteristic decay times which are driven by factors such as, trap states or charge extraction, but they do not necessarily represent the charge-carrier lifetimes for the unprotected and P3HT-protected films. Since there is no charge extraction in the unprotected film, τ_1 represents the recombination in trap states. Where as in the P3HT-protected film the decay time is dominated more by the charge extraction rather than the trap states. As charge extraction does not lead to radiative recombination, therefore the PL yield is reduced for the P3HT-protected

film compared to the unprotected film as observed by the steady-state PL measurement. Although the decay curve τ_1 for the P3HT-protected film does not prove that the charge carriers are extracted, it is the most probable mechanism since otherwise the fast decay would mean the loss of carriers in trap states. As a result, this would lead to a non-functioning device, which is not the case in our study. Faster charge extraction as well as reduced trap-induced non-radiative recombination in the interface suggests that a better interface can be obtained by incorporating a P3HT interlayer, thereby improving charge transport properties and device performance. We employed both laboratory and synchrotron XPS methods for surface-to-bulk chemical analysis (Fig. 1(I) and (J)) to realize the effect of the protection layer over the perovskite surface. Unlike the unprotected perovskite films, a distinct peak at ~71.9 eV is observed along with the Br3d (69.0 eV) and Cs3d (76.2 eV) in the XPS spectra of P3HT-protected perovskite films, with higher intensity at lower photon energy, indicating surface phenomena. This peak likely originates from an organic adduct, such as $-CH_3Br$, formed from the reaction between P3HT's $-C_6H_{13}$ side chain and excess Br during perovskite layer formation.[34] The surface-bound adduct potentially reduces dangling bonds from undercoordinated lead atoms, thereby decreasing surface recombination and enhancing interfacial charge transport and stability. For the work function (WF) analysis and corresponding binding energies (C1s, Pb4f, S2p, I3d) please refer to Fig. S7 (ESI†). We have also analysed the depth profile between the perovskite and the P3HT layer *via* the time of flight secondary ion mass spectrometry (ToF-SIMS) measurements (Fig. S8, ESI†). The ToF-SIMS measurement shows that the overall layer depth of the perovskite composition remains the same. The increase in the amount of lead at the surface may stem from the matrix effect. Notably, the presence of sulphur in the form of $-SCH^+$ species and the hydrocarbon chain (C_6H_6) was exclusively observed at the P3HT-protected surface. Additionally, a signal from a $[PbOSCH]^+$ cluster on the surface of the P3HT-protected perovskite layer is observed as reported in Fig. S8 (ESI†). Thus, the interaction between Pb^{2+} and SCH^+ on the surface appears to reduce the non-radiative recombination as well as improved stability.

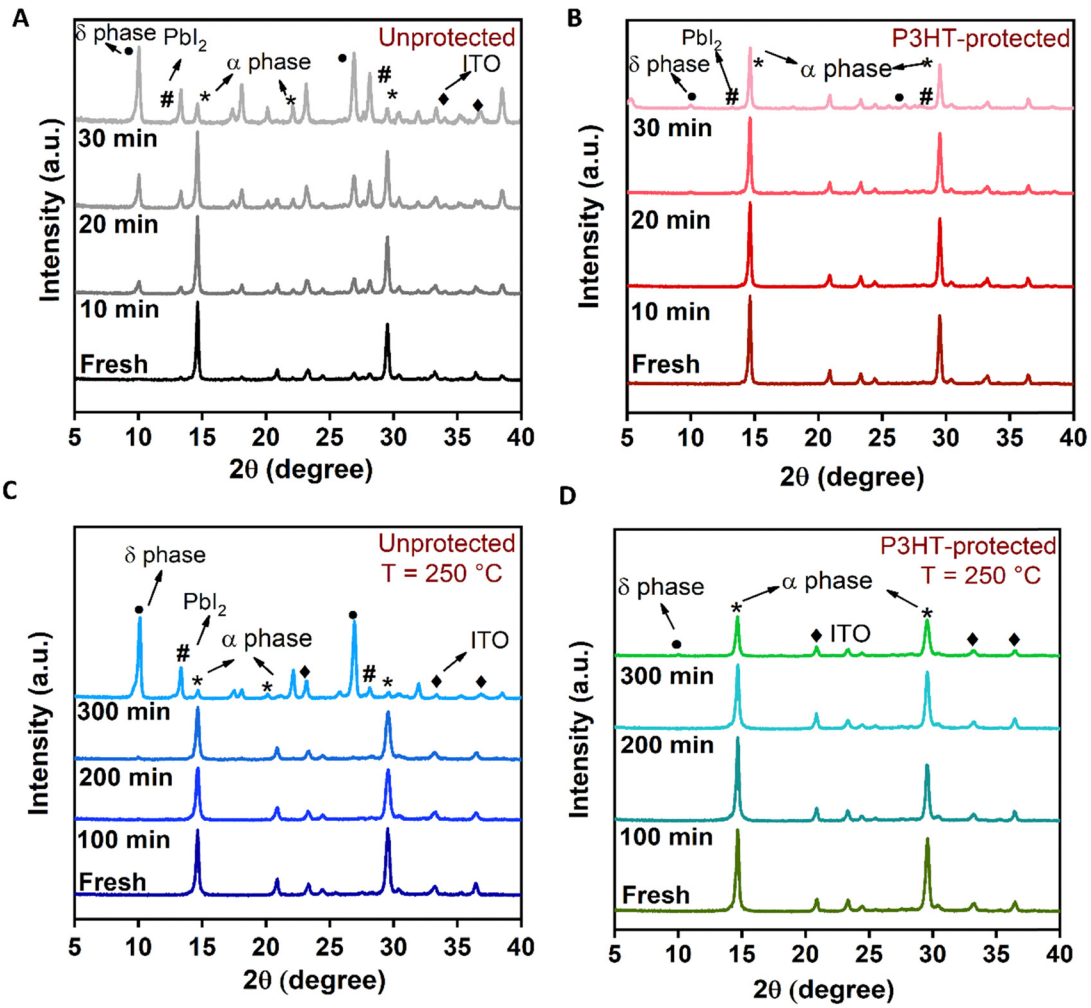

Fig. 2 XRD pattern of (A) unprotected and (B) P3HT-protected perovskite films under 60% humidity conditions, (C) and (D) unprotected and P3HT-protected perovskite films under thermal stress.

In addition to the phase stability, one of the main hurdles for the all-inorganic perovskite is stability against high temperature and humidity. Therefore, we have investigated the stability improvement of the perovskite films under different conditions, such as high humidity (~60%), high thermal stress of 250 °C, and by dipping the perovskite films in water. For the humidity test, the structural stabilities of the unprotected and P3HT-protected perovskite films were evaluated using the XRD measurements, and the results are shown in Fig. 2(A) and (B), respectively. For fresh samples, the XRD measurements are performed directly after the deposition for both the unprotected and P3HT-protected films. To test the stability of perovskite films (unprotected and P3HT-protected) against humidity, the XRD measurement was carried out after aging for 30 min (with 10 min time intervals) in a closed controlled chamber with RH ~ 60%. As can be seen in Fig. 2(A), for the unprotected films, after aging for 10 min in RH ~60%, the XRD pattern shows the appearance of the δ-phase peak at $2\theta = 10.6^\circ$ indicating the degradation of the perovskite black phase. The XRD peak intensity of δ-phase increases with further aging. After 30 min of aging, the α-phase of the perovskite deteriorates completely as the peak at $2\theta = 14.6^\circ$ significantly reduces and a strong intense peak corresponding to the degraded yellow phase appears. On the other hand, for the P3HT-protected perovskite film, the XRD pattern shows negligible change in the XRD peak intensity at $2\theta = 14.6^\circ$ and 29.8°, implying enhanced stability. Furthermore, it is worth noting that only a minimal amount of the δ-phase forms after a 30 min aging period, as shown in Fig. 2(B). Along with the δ-phase peak, the formation of the PbI_2 peak also emerges at $2\theta = 12.6^\circ$ for the unprotected devices with aging. However, in the case of the P3HT-protected films, the formation of the PbI_2 peak is negligible even after 30 min of aging. The slower formation of the δ-phase and PbI_2 peak at RH ~ 60% emphasizes the improved perovskite stability and film quality attributed to the presence of the P3HT-protection layer. This improvement is further supported by the contact angle measurement under ambient conditions as shown in Fig. S9 (ESI†). The unprotected film shows contact angle of 14.7°, implying a more hydrophilic surface, where the P3HT-protected surface is more hydrophobic with a contact angle of 93.7°.

For the thermal stability tests, the XRD is recorded by exposing the unprotected and P3HT-protected films to 250 °C under ambient humidity conditions. The results are shown in Fig. 2(C) and (D), respectively. Under high thermal stress, the unprotected perovskite films transform from the photoactive

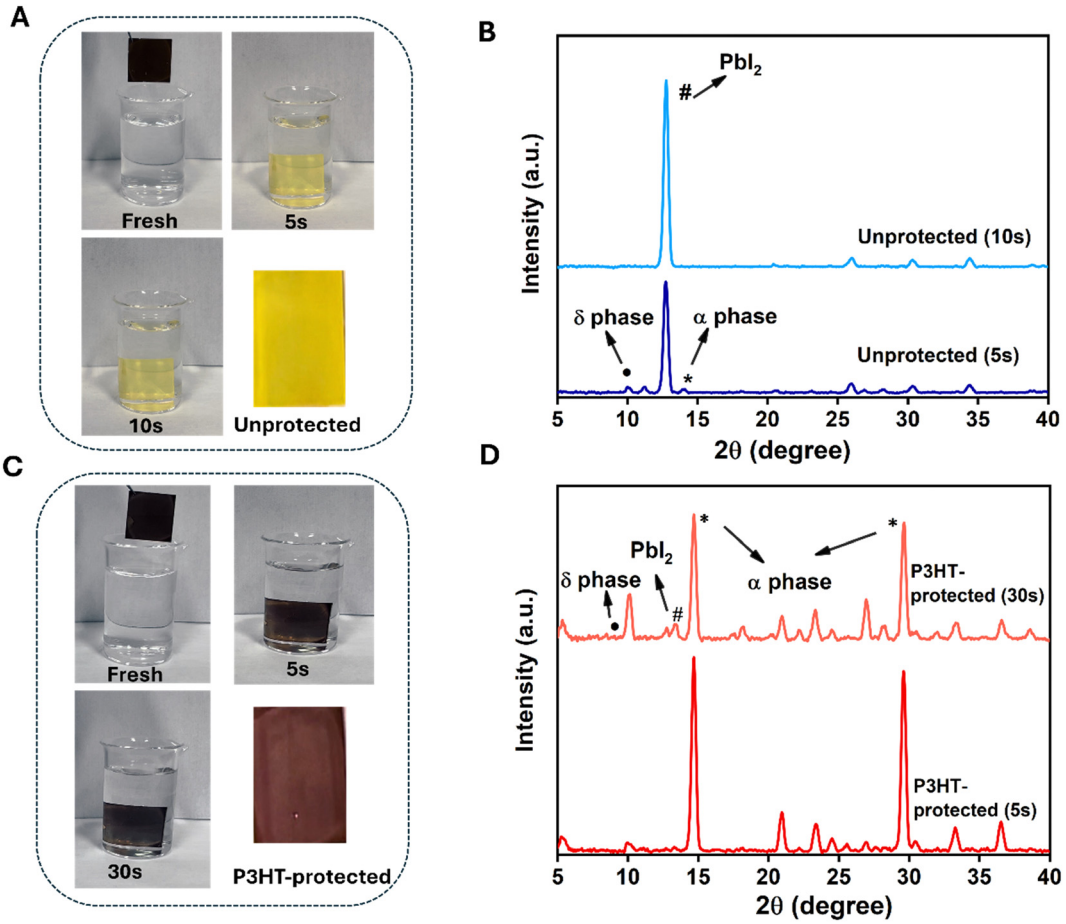

Fig. 3 (A) Water dipping test for the unprotected film, (B) XRD pattern of the unprotected film after water exposure, (C) Water dipping test for the P3HT-protected film, (D) XRD pattern of the P3HT-protected film after water exposure.

black phase to the photoinactive yellow phase while the P3HT-protected perovskite film shows a stable black phase even after 300 min of exposing to high temperature.

To access the stability enhancement through the P3HT interface engineering, we have conducted the water dipping test on the films. Fig. 3(A) and (C) show the effect of P3HT-protection layer when dipped in water compared to the unprotected. Fig. 3(B) and (D) show the XRD pattern for the unprotected and P3HT-protected films respectively after dipping in water. The P3HT-protected film has retained the perovskite layer for more than 30 s without significant change in the colour compared to the unprotected which has shown a rapid colour change from brown to yellow after 5 s submersion in water. This observation is supported by the corresponding XRD plots. Upon water dipping, the unprotected film (Fig. 3(B)) exhibited a δ-peak at 10.6° and a PbI_2 peak at 12.6° immediately, with a degraded perovskite peak at 14.6°. After 10 s, the unprotected film shows complete degradation with a highly intense PbI_2 peak. In contrast, the P3HT-protected film, after 5 s of dipping, displays only a negligible amount of degradation with a small amount of PbI_2 peak while maintaining a strong intense perovskite peak at 14.6°, indicating the additional stability provided by the P3HT interlayer (Fig. 3(D)). Continued water exposure led to a gradual degradation of the perovskite peak after 30 s for the P3HT-protected film, accompanied by the appearance of the PbI_2 peak at 12.6° and the δ-peak. This indicates that the incorporation of the P3HT-protection layer during the perovskite crystallization plays a significant role in providing additional stability to the perovskite layer by shielding it from exposure to water molecules.

The device processing is outlined and explained in Scheme 1. Fig. 4(A)–(D) represent the device statistics and shows a significant increase in all the device parameters especially in the FF. The unprotected PSCs show an average short-circuit current (J_{SC}) = (12.5 ± 0.5) mA cm^{-2} (n = 38), open-circuit voltage (V_{OC}) = (1.13 ± 0.03) V, and FF = (73.0 ± 5.0)% and PCE of (11 ± 1.7)% where the P3HT-protected devices show an average J_{SC} = (13.5 ± 0.8) mA cm^{-2} (n = 44), V_{OC} = (1.15 ± 0.6) V, FF = (79 ± 2.0)% and PCE of (11 ± 2.3)%. Fig. 4(E) shows the best-performing current density–voltage (J–V) characteristic curves of the unprotected and P3HT-protected devices (measured in a reverse scan) along with the stabilized power output (SPO) measurement over 300 s under 1-sun illumination. The best-performing device parameters for unprotected and P3HT-protected devices are presented in Table 1.

The significant FF improvement is likely due to the enhanced interfacial connection between the perovskite and the HTL *via* the P3HT-protection layer, as well as reduced surface recombination. In addition to the FF, there is also a slight increase in the photocurrent for the devices with the P3HT-protection layer (14 mA cm^{-2}), aligning well with the J_{SC} (13.6 mA cm^{-2}) obtained from the external quantum efficiency (EQE) measurement, as shown in Fig. S10 (ESI†), implying excellent hole transport capability *via* the P3HT protection and emphasizing the role of charge transport layer in enhancing the J_{SC}.[35] Additionally, to explore the impact of the

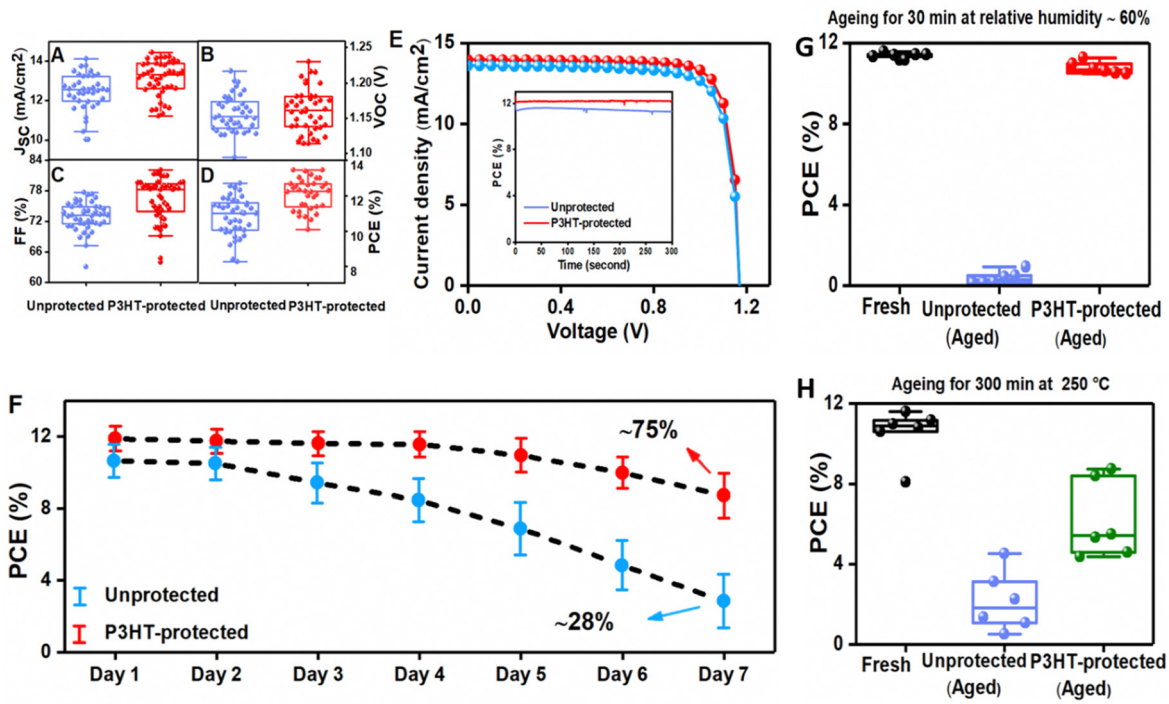

Fig. 4 (A)–(D) Device statistics (n = 38) of the unprotected and P3HT-protected devices (n = 44) for J_{sc}, V_{oc}, FF, and PCE, (E) J–V curves for the best performing unprotected and P3HT-protected device along with the stabilized power output (SPO) of the respective devices, (F) shelf life stability of the unprotected and P3HT-protected devices over 7 days of J–V measurement, (G) device statistics for the unprotected and P3HT-protected at RH ~ 60%, (H) device statistics for the unprotected and P3HT-protected under thermal stress of 250 °C.

Table 1 Measured PV parameters for the best-performing unprotected and P3HT-protected devices

Device	J_{SC} (mA cm^{-2})	V_{OC} (V)	FF (%)	PCE (%)
Unprotected	13.6	1.17	79.6	12.7
Average photovoltaic parameters	12.5 ± 0.5	1.13 ± 0.03	73.0 ± 5.0	11 ± 1.7
Median	12.55	1.15	73.31	11.00
P3HT-protected	14.0	1.17	82.2	13.5
Average photovoltaic parameters	13.5 ± 0.8	1.15 ± 0.6	79 ± 2.0	11 ± 2.3
Median	13.31	1.16	78.30	12.23

P3HT-protection layer in the presence of another HTL, devices were fabricated using spiro-MeOTAD as the HTL, as illustrated in Fig. S11 and S12 (ESI†). In addition, the device stability test has been performed under 80 °C for the P3HT-protected devices and unprotected devices (with P3HT or, spiro as HTL) as shown in Fig. S13 (ESI†). The stability test is performed in ambient condition for 450 mins retaining >90% of the $PCE_{Initial}$ and in N_2 condition for 100 h retaining ~80% of the $PCE_{Initial}$ for the P3HT-protected devices. However, the overall device performance is notably superior when using P3HT as the HTL with the P3HT-protection layer. Fig. 4(F) represents the shelf life stability of the unprotected and P3HT-protected devices over 7 days of measurement in ambient humidity conditions. P3HT-protected devices have retained ~75% of their initial PCE, while the unprotected devices retain only ~28% of their initial value. To further understand the effect of stability on the device performance, we have fabricated $CsPbI_2Br$ devices based on unprotected and P3HT-protected films under RH ~60%. P3HT-protected perovskite films retained ~90% of the initial PCE while the unprotected devices completely degraded after the aging test as shown in Fig. 4(G). This corroborates the XRD pattern (Fig. 2(A) and (B)) and signifies the importance of the P3HT-protecttion layer to enhance the stability of the inorganic perovskite against high humidity atmosphere. To understand the prolonged stability of P3HT-protected perovskite thin films, we fabricated devices with perovskites exposed to 250 °C and performed the thermal *J–V* measurements in Fig. 4(H). As can be seen, the aged P3HT-protected device still retained more than 50% of its initial PCE after aging for 300 min whereas for the unprotected devices, the average PCE decreased to less than 25% after the thermal aging test. These results correspond well with the thermal XRD data as shown earlier in Fig. 2(C) and (D) followed by gives us a strong implication on the stability improvement with the P3HT-protection layer under robust conditions and stress factors. The role of P3HT-protection layer is further tested over devices with spiro HTL at RH ~ 60% (for 30 min) and temperature at 80 °C (for 300 min) as shown in S14 (ESI†). The devices with P3HT-protection showed extensive stability where under both conditions the unprotected devices rapidly degraded, implying the efficacy of the interface engineering strategy over other HTM.

Conclusion

Our study develops an interface strategy for enhancing the stability of the all-inorganic perovskite composition ($CsPbI_2Br$). The deposition of a thin P3HT-protection layer between the perovskite and the hole transport layer proved to be instrumental in improving the film morphology and crystallinity as evident from the SEM and XRD analyses, respectively. ToF-SIMS studies reveal the presence of P3HT layer only on top of the perovskite layer with no traces in the bulk. XPS analysis, along with the PL and TRPL results, shows a significant reduction in surface recombination and overall enhancement in the interfacial charge transport properties and FF up to 82.2%. XRD tests under humidity (RH ~ 60%) demonstrate a significant slowdown in the α- to δ-phase transition for the P3HT-protected films which is reflected in the device performances, retaining a 90% of their original PCE. Thermal XRD tests at 250 °C, supported by device performance under similar conditions, show the P3HT-protected devices retain more than 50% of their initial PCE value upon 300 min of the aging test. The water dipping test provides clear evidence of the homogeneous surface coverage achieved through P3HT interface strategy, resulting in a more stable perovskite absorber layer. Our findings present an effective route to enhance the stability of the $CsPbI_2Br$ perovskite solar cells against moisture and high temperature, which are among the main stability challenges for perovskites.

Author contributions

M. Saliba directed and supervised the research. M. Saliba, M. M. Byranvand, R. Roy conceived the idea. R. Roy designed the experiments and responsible for device and film fabrication as well as data interpretation. M. R. Zohdi helped measuring XRD. Theresa M. F. and M. Rai measured SEM. W. Zuo helped with the schematic. W. Hempel measured ToF-SIMS and interpreted the data. M. Kedia helped with AFM measurements. J. J. Rendon assisted the water stability test. S. Boehringer assisted the PL measurement. C. Das, M. Vorochta & S. Mehl performed the XPS measurements. S. Mathur participated with the project discussions. R. Roy wrote the first draft of the manuscript under the guidance of M. Saliba. All co-authors participated in the discussion and commented, reviewed and approved the paper. A. Kulkarni, M. M. Byranvand and M. Saliba provided expertise and supervised the work.

Data availability

The data supporting the article have been included as part of the ESI.†

Conflicts of interest

There are no conflicts to declare.

Acknowledgements

M. S. and R. R. acknowledge funding by ProperPhotoMile. Project ProperPhotoMile is supported under the umbrella of SOLAR-ERA.NET Cofund 2 by the Spanish Ministry of Science and Education and the AEI under the project PCI2020-112185 and CDTI project number IDI-20210171; the Federal Ministry for Economic Affairs and Energy on the basis of a decision by the German Bundestag project numbers FKZ 03EE1070B and FKZ 03EE1070A and the Israel Ministry of Energy with project number 220-11-031. SOLAR-ERA.NET is supported by the European Commission within the EU Framework Programme for Research and Innovation HORIZON 2020 (Cofund ERA-NET Action, No. 786483), funded by the European Union. The views and opinions expressed are, however, those of the author(s) only and do not necessarily reflect those of the European Union or the European Research Council Executive Agency (ERCEA). Neither the European Union nor the granting authority can be held responsible for them. The authors acknowledge funding from the European Research Council under the Horizon Europe program (LOCAL-HEAT, grant agreement no. 101041809). M. S. and M. K. thanks the German Research Foundation (DFG) for funding (SPP2196, 431314977/GRK 2642). M. S. acknowledges funding from the German Bundesministerium für Bildung and Forschung (BMBF), project "NETPEC" (01LS2103E). A.K. acknowledge support from Deutscher Akademischer Austauschdiensts through a DAAD-PRIME fellowship under the ST43 – Research Fellowship Programmes. M.V acknowledges support from the Czech Ministry of Education, Youth and Sports under the project LM2023072. The authors also thank Somayeh Gholipour for technical assistance.

References

1 A. Kojima, K. Teshima, Y. Shirai and T. Miyasaka, Organometal halide perovskites as visible-light sensitizers for photovoltaic cells, *J. Am. Chem. Soc.*, 2009, **131**(17), 6050–6051.

2 National Renewable Energy Laboratory. Best Research-Cell Efficiency Chart | Photovoltaic Research|NREL. **https://www.nrel.gov/pv/cell-efficiency.html**, 2022.

3 F. He, W. Xu, M. Zhang, X. Zhang, B. Ding, G. Wei and F. Kang, Highly Crystalline $CsPbI_2Br$ Films for Efficient Perovskite Solar Cells *via* Compositional Engineering, *RSC Adv.*, 2019, **9**, 30534–30540.

4 Y. Chen, T. Shi, P. Liu, W. Xie, K. Chen, X. Xu, L. Shui, C. Shang, Z. Chen and H.-L. Yip, *et al.*, The Distinctive Phase Stability and Defect Physics in $CsPbI_2Br$ Perovskite, *J. Mater. Chem. A*, 2019, **7**, 20201–20207.

5 D. Bai, H. Bian, Z. Jin, H. Wang, L. Meng, Q. Wang and S. (Frank) Liu, Temperature-Assisted Crystallization for Inorganic $CsPbI_2Br$ Perovskite Solar Cells to Attain High Stabilized Efficiency 14.81%, *Nano Energy*, 2018, **52**, 408–415.

6 C. Dong, X. Han, W. Li, Q. Qiu and J. Wang, Anti-Solvent Assisted Multi-Step Deposition for Efficient and Stable Carbon-Based $CsPbI_2Br$ All-Inorganic Perovskite Solar Cell, *Nano Energy*, 2019, **59**, 553–559.

7 C. Liu, W. Li, C. Zhang, Y. Ma, J. Fan and Y. Mai, All-Inorganic $CsPbI_2Br$ Perovskite Solar Cells with High Efficiency Exceeding 13%, *J. Am. Chem. Soc.*, 2018, **140**, 3825–3828.

8 F. Deng, X. Li, X. Lv, J. Zhou, Y. Chen, X. Sun, Y.-Z. Zheng, X. Tao and J.-F. Chen, Low-Temperature Processing All-Inorganic Carbon-Based Perovskite Solar Cells up to 11.78% Efficiency *via* Alkali Hydroxides Interfacial Engineering, *ACS Appl. Energy Mater.*, 2019, **3**, 401–410.

9 J. Zhang, Z. Jin, L. Liang, H. Wang, D. Bai, H. Bian, K. Wang, Q. Wang, N. Yuan and J. Ding, *et al.*, Iodine-optimized Interface for Inorganic $CsPbI_2Br$ Perovskite Solar Cell to Attain High Stabilized Efficiency Exceeding 14%, *Adv. Sci.*, 2018, **5**(12), 1801123.

10 C. F. Lau, M. Zhang, X. Deng, J. Zheng, J. Bing, Q. Ma, J. Kim, L. Hu, M. A. Green and S. Huang, *et al.*, Strontium-Doped Low-Temperature-Processed $CsPbI_2Br$ Perovskite Solar Cells, *ACS Energy Lett.*, 2017, **2**, 2319–2325.

11 L. Zhou, X. Guo, Z. Lin, J. Ma, J. Su, Z. Hu, C. Zhang, S. F. Liu, J. Chang and Y. Hao, Interface Engineering of Low Temperature Processed All-Inorganic $CsPbI_2Br$ Perovskite Solar Cells toward PCE Exceeding 14%, *Nano Energy*, 2019, **60**, 583–590.

12 J. Li, J. Yang, J. Ma, J. Liang, Y. Liu, X. Hu, C. Chen, W. Yang, J. Min and Q. Bao, *et al.*, Minimizing Open-Circuit Voltage Deficit *via* Interface Engineering for Highly Efficient $CsPbI_2Br$ Perovskite Solar Cells, *Chem. Eng. J.*, 2021, **417**, 129247.

13 J. Yuan, L. Zhang, C. Bi, M. Wang and J. Tian, Surface Trap States Passivation for High-performance Inorganic Perovskite Solar Cells, *Sol. RRL*, 2018, **2**(10), 1800188.

14 A. K. Jena, A. Kulkarni, Y. Sanehira, M. Ikegami and T. Miyasaka, Stabilization of α-$CsPbI_3$ in Ambient Room Temperature Conditions by Incorporating EU into $CsPbI_3$, *Chem. Mater.*, 2018, **30**, 6668–6674.

15 S. Öz, A. K. Jena, A. Kulkarni, K. Mouri, T. Yokoyama, I. Takei, F. Ünlü, S. Mathur and T. Miyasaka, Lead(II) Propionate Additive and a Dopant-Free Polymer Hole Transport Material for $CsPbI_2Br$ Perovskite Solar Cells, *ACS Energy Lett.*, 2020, **5**, 1292–1299.

16 E. J. Juarez-Perez, L. K. Ono, I. Uriarte, E. J. Cocinero and Y. Qi, Degradation mechanism and relative stability of methylammonium halide based perovskites analyzed on the basis of acid–base theory, *ACS Appl. Mater. Interfaces*, 2019, **11**, 12586–12593.

17 C. Liu, X. Sun, Y. Yang, O. A. Syzgantseva, M. A. Syzgantseva, B. Ding, N. Shibayama, H. Kanda, F. Fadaei Tirani and R. Scopelliti, Retarding Solid-State Reactions Enable Efficient and Stable All-Inorganic Perovskite Solar Cells and Modules, *Sci. Adv.*, 2023, **9**(21), eadg0087.

18 Z. Iqbal, R. Félix, A. Musiienko, J. Thiesbrummel, H. Köbler, E. Gutierrez-Partida, T. W. Gries, E. Hüsam, A. Saleh and

R. G. Wilks, *et al.*, Unveiling the Potential of Ambient Air Annealing for Highly Efficient Inorganic CSPBI3 Perovskite Solar Cells, *J. Am. Chem. Soc.*, 2024, **146**, 4642–4651.

19 Y. Ding, Q. Guo, Y. Geng, Z. Dai, Z. Wang, Z. Chen, Q. Guo, Z. Zheng, Y. Li and E. Zhou, A Low-Cost Hole Transport Layer Enables $CsPbI_2Br$ Single-Junction and Tandem Perovskite Solar Cells with Record Efficiencies of 17.8% and 21.4%, *Nano Today*, 2022, **46**, 101586.

20 S. Shan, C. Xu, H. Wu, B. Niu, W. Fu, L. Zuo and H. Chen, Manipulating the Crystallization and Phase Transition for High-performance $CsPbI_2Br$ Solar Cells, *Adv. Energy Mater.*, 2022, **13**(6), 2203682.

21 W. Xiang, S. Liu and W. A. (Frank) Tress, Review on the Stability of Inorganic Metal Halide Perovskites: Challenges and Opportunities for Stable Solar Cells, *Energy Environ. Sci.*, 2021, **14**, 2090–2113.

22 W. Xiang, Z. Wang, D. J. Kubicki, X. Wang, W. Tress, J. Luo, J. Zhang, A. Hofstetter, L. Zhang, L. Emsley, M. Grätzel and A. Hagfeldt, BA-induced phase segregation and band gap reduction in mixed-halide inorganic perovskite solar cells, *Nat. Commun.*, 2019, **10**(1), 2203682.

23 T. Ozturk, E. Akman, A. E. Shalan and S. Akin, Composition engineering of operationally stable $CsPbI_2Br$ perovskite solar cells with a record efficiency over 17%, *Nano Energy*, 2021, **87**, 106157.

24 M. M. Byranvand, T. Kodalle, W. Zuo, T. Magorian Friedlmeier, M. Abdelsamie, K. Hong, W. Zia, S. Perween, O. Clemens, C. M. Sutter-Fella and M. Saliba, One-step thermal gradient- and antisolvent-free crystallization of all-inorganic perovskites for highly efficient and thermally stable solar cells, *Adv. Sci.*, 2022, **9**(23), 2202441.

25 P. Wang, H. Wang, Y. Mao, H. Zhang, F. Ye, D. Liu and T. Wang, Organic Ligands Armored Zno Enhances Efficiency and Stability of $CsPbI_2Br$ Perovskite Solar Cells, *Adv. Sci.*, 2020, **7**(21), 2000421.

26 J. He, J. Liu, Y. Hou, Y. Wang, S. Yang and H. G. Yang, Surface Chelation of Cesium Halide Perovskite by Dithiocarbamate for Efficient and Stable Solar Cells, *Nat. Commun.*, 2020, **11**, 4237.

27 S. Shan, C. Xu, H. Wu, B. Niu, W. Fu, L. Zuo and H. Chen, Manipulating the Crystallization and Phase Transition for High-performance $CsPbI_2Br$ Solar Cells, *Adv. Energy Mater.*, 2022, **13**(6), 2203682.

28 M. H. Li, J. Y. Shao, Y. Jiang, F. Z. Qiu, S. Wang, J. Zhang, G. Han, J. Tang, F. Wang, Z. Wei, Y. Yi, Y. W. Zhong and J. S. Hu, Electrical loss management by molecularly manipulating Dopant-Free Poly(3-hexylthiophene) towards 16.93% $CsPbI_2Br$ solar cells, *Angew. Chem., Int. Ed.*, 2021, **60**(30), 16388–16393.

29 X. Liu, J. Li, X. Cui, X. Wang and D. Yang, The Progress and Efficiency of $CsPbI_2Br$ Perovskite Solar Cells, *J. Mater. Chem. C*, 2023, **11**, 426–455.

30 Y. Han, H. Zhao, C. Duan, S. Yang, Z. Yang, Z. Liu and S. F. Liu, Controlled n-doping in air-stable $CsPbI_2Br$ perovskite solar cells with a record efficiency of 16.79%, *Adv. Funct. Mater.*, 2020, **30**(12), 1909972.

31 W. Zhang, J. Xiong, J. Li and W. A. Daoud, Guanidinium passivation for air-stable rubidium-incorporated $Cs_{(1-x)}Rb_xPbI_2Br$ inorganic perovskite solar cells, *Sol. RRL*, 2020, **4**(6), 2000112.

32 K. Zheng, J. Ge, C. Liu, Q. Lou, X. Chen, Y. Meng, X. Yin, S. Bu, C. Liu and Z. Ge, Improved Phase Stability of $CsPbI_2Br$ Perovskite by Released Microstrain toward Highly Efficient and Stable Solar Cells, *InfoMat*, 2021, **3**, 1431–1444.

33 F. Yang, D. Hirotani, G. Kapil, M. A. Kamarudin, C. H. Ng, Y. Zhang, Q. Shen and S. Hayase, All-inorganic $CsPb_{1-x}Ge_xI_2Br$ Perovskite with Enhanced Phase Stability and Photovoltaic Performance, *Angew. Chem., Int. Ed.*, 2018, **57**, 12745–12749.

34 B. Chaudhary, A. Kulkarni, A. K. Jena, M. Ikegami, Y. Udagawa, H. Kunugita, K. Ema and T. Miyasaka, Poly(4-vinylpyridine)-based Interfacial Passivation to Enhance Voltage and Moisture Stability of Lead Halide Perovskite Solar Cells, *ChemSusChem*, 2017, **10**, 2473–2479.

35 S. Akel, A. Kulkarni, U. Rau and T. Kirchartz, Relevance of Long Diffusion Lengths for Efficient Halide Perovskite Solar Cells, *PRX Energy*, 2023, **2**, 013004.

